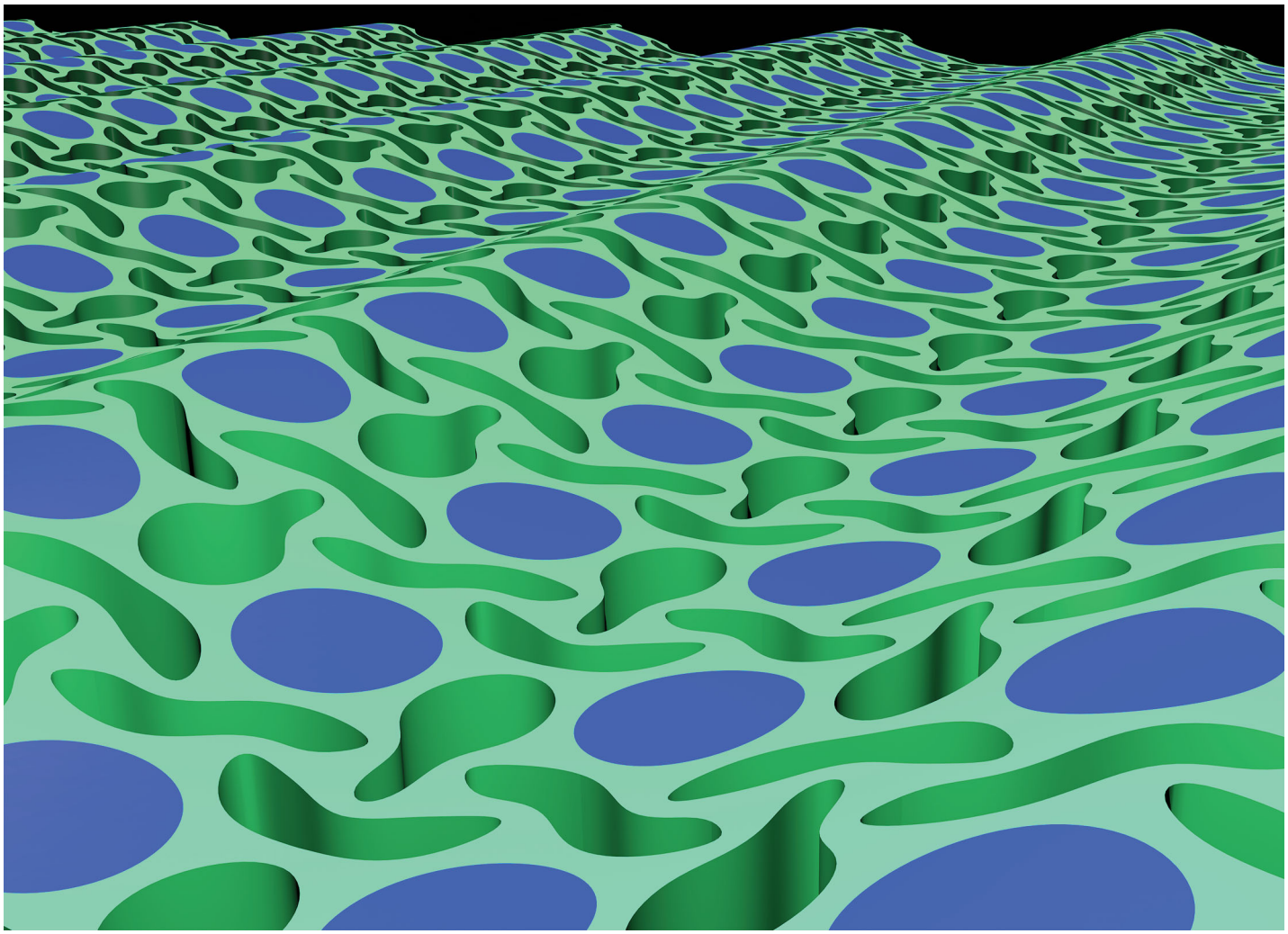
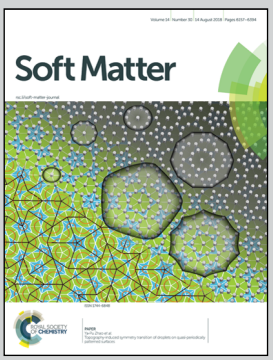


Highlighting research from the University of Wisconsin – Madison, and Technion.

Auxetic multiphase soft composite material design through instabilities with application for acoustic metamaterials

This work presents instability induced switchable Negative Poisson's ratio or auxetic behavior in 3D-printed multiphase soft composites. We show how the auxetic behavior can be controlled through positioning of stiff inclusions combined with periodically distributed voids in soft matrix. We apply these reversible pattern transformations for controlling elastic waves. Through numerical simulations, we illustrate the capability of the tunable metamaterials to cancel low frequency ranges controlled by deformation.

As featured in:



See Stephan Rudykh *et al.*, *Soft Matter*, 2018, **14**, 6171.

ROYAL SOCIETY OF CHEMISTRY

rsc.li/soft-matter-journal

Registered charity number: 207890

Soft Matter

COMMUNICATION

View Article Online
View Journal | View Issue

Published on 11 July 2018. Downloaded by Albert Ludwigs Universitaet Freiburg on 4/29/2023 10:40:51 PM.

Check for updates

Cite this: *Soft Matter*, 2018, **14**, 6171

Received 28th April 2018,
Accepted 10th July 2018

DOI: 10.1039/c8sm00874d

rsc.li/soft-matter-journal

Auxetic multiphase soft composite material design through instabilities with application for acoustic metamaterials

Jian Li,[a] Viacheslav Slesarenko[a] and Stephan Rudykh *[b]

We investigate the instability-induced pattern transformations in 3D-printed soft composites consisting of stiff inclusions and voids periodically distributed in a soft matrix. These soft auxetic composites are prone to elastic instabilities giving rise to negative Poisson's ratio (NPR) behavior. Upon reaching the instability point, the composite microstructure rearranges into a new morphology attaining an NPR regime. Remarkably, identical composites can morph into distinct patterns depending on the loading direction. These fully determined instability-induced distinct patterns are characterized by significantly different NPR behaviors, thus, giving rise to enhanced tunability of the composite properties. Finally, we illustrate a potential application of these reversible pattern transformations as tunable acoustic-elastic metamaterials capable of selectively filtering low frequency ranges controlled by deformation.

Auxetic materials, also known as materials with negative Poisson's ratio (NPR), are characterized by their unusual response to uniaxial strain. Opposite to conventional materials, they demonstrate lateral shrinkage while being compressed. This endows auxetic materials with many desirable properties, such as enhanced mechanical resistance,[1,2] variable permeability,[3,4] high energy absorption ability[5] and synclastic behavior.[6] Due to these remarkable properties, auxetic materials can be potentially used in various applications, including protective devices,[7] smart sensors[8] and filters,[3,9] angioplasty stents,[10] fasteners[11] and textiles.[12] Among them, perforated systems[13–15] are of particular interest thanks to their relative simplicity and low cost of manufacturing; for example, various periodic patterns, ranging from diamonds[16] to stars[17] or slits,[18–20] have been explored to design auxetic materials. Meanwhile, there has been increasing interest in using elastic instability induced pattern transformations to design reconfigurable metamaterials that exhibit negative Poisson's ratio behavior.[21]

Bertoldi *et al.*[22] illustrated the NPR behavior in two-dimensional periodic porous structures with square arrays of circular voids in an elastomeric matrix. They found that the auxetic behavior arose from the dramatic changes in geometry due to the development of elastic instability. Overvelde *et al.*[23] considered the effect of pore shape on the mechanical response; Shim *et al.*[24] systematically investigated the role of circular hole arrangement on the post-buckling behavior of the periodic porous structures. Remarkably, these reversible pattern transformations have been demonstrated to be instrumental to design tunable color displays,[25,26] and phononic[27–29] and photonic[30] switches. The design of the periodic elastomeric porous structures is based on various distributions of voids in a single phase matrix material. Furthermore, mechanical properties[31] and surface patterns[32] in stiff-soft two phase composites can be controlled by tailored stiff phase distributions.

Here, we put forward a new design of soft auxetic composites incorporating stiff inclusions and voids periodically distributed in the soft matrix. The rich design space of the material system provides the means to control the onset of instabilities and pattern formations through the positioning of the stiff phase, while maintaining the ability to pre-design collapse of the voids. This combination of voids, soft and stiff phases gives rise to new admissible multiple pattern switches, and tunable and enhanced NPR behavior. Guided by our numerical simulations, we experimentally realize the instability-induced pattern transformations and the NPR behavior in 3D-printed multiphase soft auxetic composites. In addition, we illustrate a potential application of the reported pattern transformation phenomenon for the design of acoustic soft metamaterials possessing tunable stop bands at low frequencies of elastic waves.

1. Material fabrication and experiments

The periodic composite specimens were fabricated by using an Object Connex 260-3 3D printer. The 3D printed samples were composed of stiff circular inclusions and voids periodically

[a] *Faculty of Aerospace Engineering, Technion – Israel Institute of Technology, Haifa 32000, Israel*
[b] *Department of Mechanical Engineering, University of Wisconsin – Madison, Madison, WI 53706, USA. E-mail: rudykh@wisc.edu*

Published on 11 July 2018. Downloaded by Albert Ludwigs Universitaet Freiburg on 4/29/2023 10:40:51 PM.

distributed in the soft matrix as schematically shown in Fig. 1. The radius of the circular voids and stiff inclusions was r_0 = 2 mm, and the initial matrix volume fraction was $c^{(m)}$ = 0.3. The stiff inclusions were printed using Verowhite resin, while the soft matrix was printed using FLX9860 digital material, which is a mixture of soft TangoBlackPlus (~85 wt%) and stiff Verowhite (~15 wt%).[33] The out-of-plane thickness of both specimens was t = 10 mm. Uniaxial compression tests were performed using a Shimadzu EZ-LX testing machine (maximum load 2 kN). During the test, the specimens were placed in a transparent fixture to prevent out-of-plane deformation. The specimens were quasi-statically compressed at a constant strain-rate of 2×10^{-4} s^{-1}. Since the microstructure exhibits different mechanical responses in the X- and Y-directions, two sets of experiments – compression in the X-, and Y-directions – were performed. The specimens that were loaded in the X or Y material direction were composed of 8×11 or 10×9 unit cells, respectively. The deformation process was recorded using a high resolution digital camera.

2. Numerical simulations

Numerical simulations are performed by means of the finite element code COMSOL 5.2a, in which the unit cell (see Fig. 1) is constructed and the corresponding periodic displacement boundary conditions are imposed on the opposite sides of the unit cell. Note that here we consider a 2D-system, in particular, plane-strain conditions are used; similar conditions are maintained in the experimental setting. The matrix and inclusion materials are modeled as neo-Hookean materials with initial shear moduli of $\mu^{(m)}$ = 0.60 MPa and $\mu^{(i)}$ = 0.63 GPa, respectively. The onset of instability is identified by Bloch–Floquet analysis superimposed on the deformed state;[27] the analysis allows us to identify the critical strain and the corresponding patterns that are formed upon achieving the critical level of deformation. This information is used in the post-buckling numerical analysis, for which new unit cells are constructed to match the new instability-induced periodicity. In particular, an enlarged unit cell consisting of 1×2 primitive unit cells with small amplitude geometrical imperfections in the form of the buckling mode (obtained by Bloch–Floquet instability analysis) is numerically analyzed in the post-buckling regime.

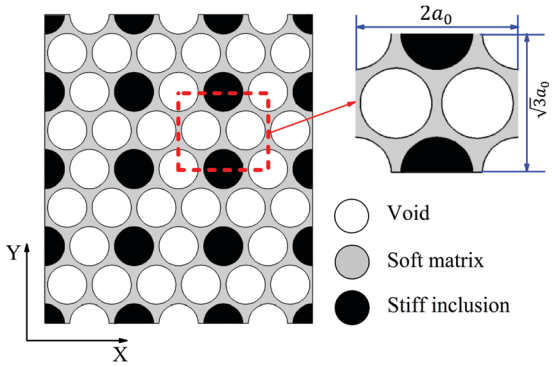


Fig. 1 Schematic of the geometric arrangement of the three phase (stiff inclusions, voids and soft matrix) periodic composites. a_0 denotes the center-to-center distance between circular voids in the undeformed configuration.

3. Results

Fig. 2 presents the evolution of the instability-induced pattern transformation when the composite is loaded in the Y (a and b) or X (c and d) material directions at different strain levels from 0 to 20% (from left to right); rows (a and d) and (b and c) show the numerical and experimental results, respectively. We observe that when the critical compressive strain is reached, the material microstructure experiences rapid and dramatic changes, leading to formation of the new patterns (see Fig. 2b and c at ε = 0.05), which further evolve with an increase in the applied strain. These observed changes in pattern transformation may be a result of a combination of the geometry changes and inhomogeneous deformation of the nonlinear materials. In particular, we note that the pattern transformation results in significant rotation of the stiff inclusion accompanied by the corresponding local deformation of the matrix. A similar deformation mechanism has been utilized in the design of functional metamaterials.[14,16,22,26,34] Note that, in agreement with the numerical instability analysis predictions, the periodicity of the new pattern doubles in the Y-direction (regardless of the compression direction). Although the development of the instability-induced patterns for the composites loaded in the X- or Y-direction is initially similar (see Fig. 2a and d at ε = 0.05), their patterns are essentially distinct at larger strain levels (for details, see the visualization of the deformed configurations in Appendix 1). The difference in the achieved distinct microstructures is dictated by the positions of the stiff inclusions relative to the loading direction. Thus, various stiff inclusion distributions give rise to an increased variety of admissible instability-triggered patterns. We note that the initial shape of the material microstructure can be fully recovered after unloading, demonstrating that these pattern transformations are fully reversible. Remarkably, the structure exhibits a negative Poisson's ratio (NPR) behavior upon developing the new instability-induced pattern; in particular, significant lateral contractions (in response to vertical contraction) are predicted numerically, and are observed experimentally (see Fig. 2b and c at ε = 0.2) for both loading cases.

Fig. 3 shows the evolutions of stress (a) and Poisson's ratio (c and d) as functions of the applied compressive strain for the composite structures loaded in the X- and Y-material directions. Both experiments and simulations indicate that the stress–strain curves are strongly affected by elastic instabilities (see Fig. 3a). In the stable regime, the stress–strain curves are almost linear, and the periodic composite exhibits different responses when loaded in the X- and Y-direction. In particular, the effective moduli are 0.46 MPa (for the X-material direction) and 0.64 MPa (for the Y-direction). While the corresponding inclusion-matrix composite with a hexagonal periodic unit cell exhibits similar in-plane responses for the corresponding X- and Y-loading directions;[35]

 This journal is © The Royal Society of Chemistry 2018

Published on 11 July 2018. Downloaded by Albert Ludwigs Universitaet Freiburg on 4/29/2023 10:40:51 PM.

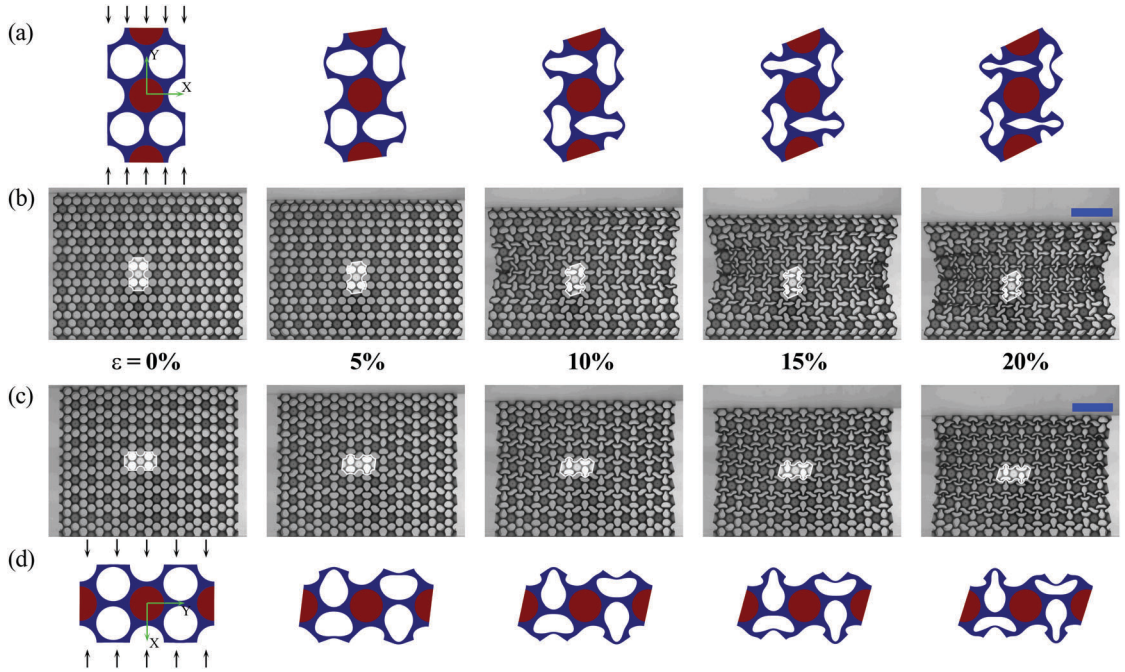


Fig. 2 Numerical and experimental images of the structure loaded in the *Y*-direction (a and b) and *X*-direction (c and d) at different macroscopic deformation levels. Scale bar: 20 mm.

the considered void–matrix–inclusion system possesses in-plane anisotropy as the microstructure differs in the *X*- and *Y*-material directions. For completeness, we show the dependence of the effective Young's moduli of the composite loaded in the *X*- and *Y*-material directions on the matrix volume fraction in Appendix 2. The critical strain levels are $\varepsilon_X^{(cr)} \approx 0.028$ for the composite loaded in the *X* material direction; and $\varepsilon_Y^{(cr)} \approx 0.039$ for the composite loaded in the *Y* material direction. The critical strain values are obtained numerically by the Bloch–Floquet analysis superimposed on the deformed state.[27] When the applied strain exceeds the critical level, significant softening of the structure is observed for both material loading directions. The numerical simulations predict earlier developments of instability patterns, as compared to the observed onset of instabilities in experiments. In addition, a drop in the stress level is observed (after the critical strain level) in experiments. This difference is due to the boundary effects of the tested samples; these effects are not included in the numerical simulations, in which infinite composites are examined through consideration of the periodic unit cell. Similar behaviors were also observed in the buckling of porous structures.[36,37] In addition, the effect of friction between the fixtures and specimens may also contribute to the appearance of the local peak in the stress–strain curve.

Remarkably, the onset of instability and the associated composite microstructure switches significantly affect the effective Poisson's ratio (see Fig. 3c and d). We observe that prior to instability, Poisson's ratio is positive in the composite loaded either in the *X*- or *Y*-material direction.† When the critical deformation is reached, the voids suddenly collapse inward leading to rapid decrease in the composite Poisson's ratio, which soon becomes negative. Further increase in compressive deformation results in a slow decrease of the Poisson's ratio. The composite structure loaded in the *X* or *Y* material direction exhibits a significant difference in the values of Poisson's ratio; for example, $\upsilon_{YX} \approx -0.2$ or $\upsilon_{XY} \approx -0.6$ at $\varepsilon = 0.2$, respectively. To highlight the significance of the stiff phase presence on the induced negative Poisson's ratio behavior, we present our numerical results for the corresponding void–matrix system (without stiff inclusions), whose buckled patterns have been experimentally observed by Shan *et al.*[24,38] The dependence of the Poisson's ratio on deformation for the void–matrix system is denoted by dash-dotted blue curves in Fig. 3c and d. We observe that the void–matrix system is characterized by positive Poisson's ratio and NPR behavior is not observed until the deformation reaches a level of $\varepsilon \approx 0.2$ (for both cases loaded in the *X*- or *Y*-direction). This is in contrast to the NPR behavior in the composites that start showing the negative values of Poisson's ratio after only $\varepsilon \approx 0.05$. Thus, at larger strain levels the periodic composites show very significant NPR behavior as compared to the corresponding void-matrix system, for example, at $\varepsilon = 0.2$, the composite shows $\upsilon_{YX} \approx -0.2$ or $\upsilon_{XY} \approx -0.6$, while the void–matrix system has a positive value for $\upsilon_{YX} \approx 0.01$, and only $\upsilon_{XY} \approx -0.03$. Furthermore, the stiff phase makes the composite prone to elastic instabilities at smaller strains; in particular, the composite experiences instabilities at only $\varepsilon_X^{(cr)} \approx 0.028$ or $\varepsilon_Y^{(cr)} \approx 0.039$; while the void-matrix material requires $\varepsilon_X^{(cr)} \approx 0.120$ or $\varepsilon_Y^{(cr)} \approx 0.078$ to buckle. Thus, our results indicate that by introducing the periodically distributed stiff phase into soft porous structures, new patterns can be induced upon instabilities; and these distinct patterns exhibit very different NPR behaviors.

Next, we show an example of the dependence of critical strain and Poisson's ratio on shear modulus contrast $\mu^{(i)}/\mu^{(m)}$

Published on 11 July 2018. Downloaded by Albert Ludwigs Universitaet Freiburg on 4/29/2023 10:40:51 PM.

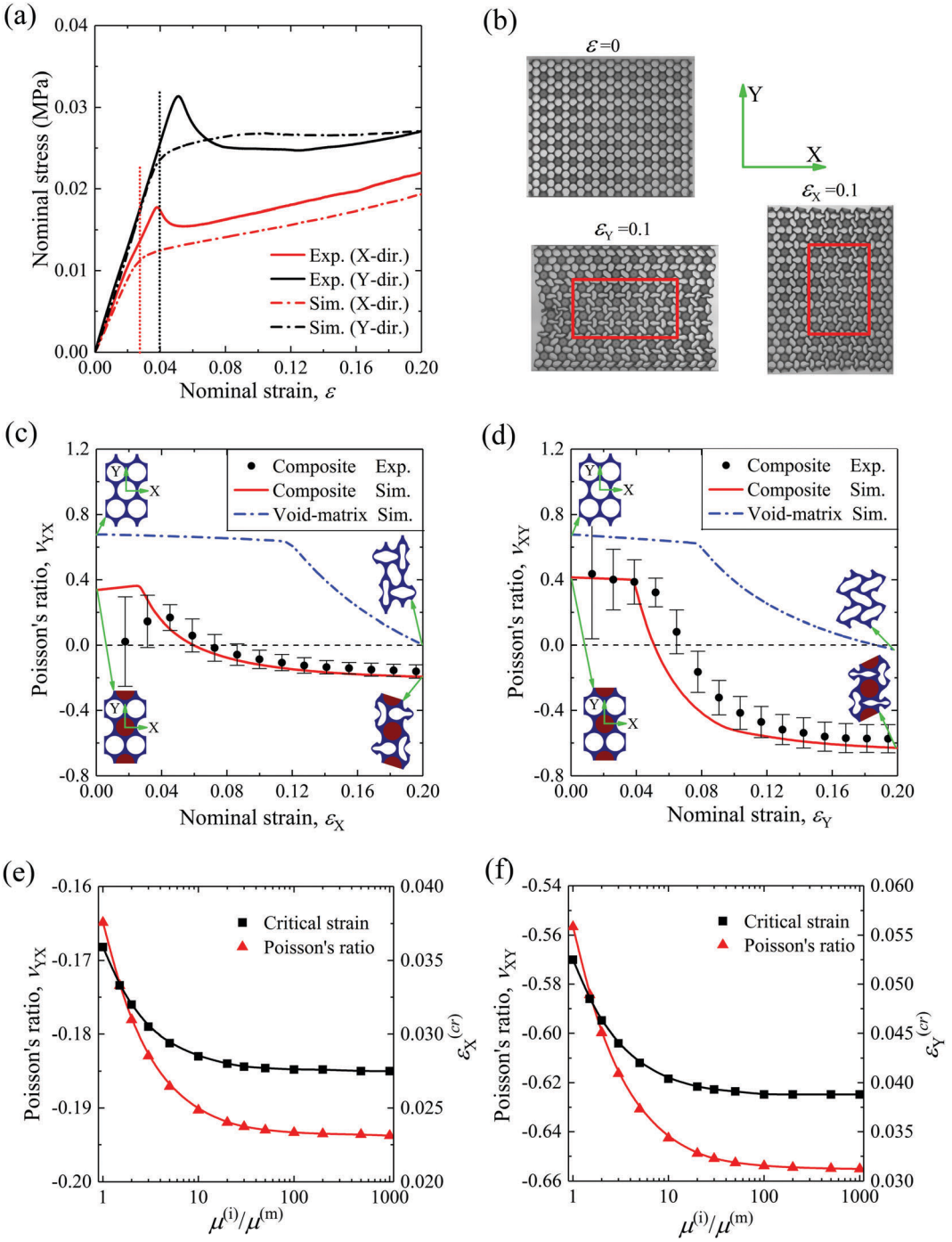


Fig. 3 (a) Numerical and experimental stress–strain curves for the structure loaded in the *Y* or *X* material direction. (b) Schematic composite areas for Poisson's ratio evaluation. (c) Poisson's ratio ν_{YX} as a function of ε_X. (d) Poisson's ratio ν_{XY} as a function of ε_Y. (e and f) Dependence of the critical strain and Poisson's ratio (at a deformation level $\varepsilon = 0.2$) on shear modulus contrast $\mu^{(i)}/\mu^{(m)}$.

in Fig. 3e and f. The example of the Poisson's ratio dependence is given for the deformation level $\varepsilon = 0.2$. Through simulations, we observe that the composites form new periodicity with 1×2 primitive unit cells for the considered range of shear modulus contrasts, $\mu^{(i)}/\mu^{(m)}$ from 1 to 1000. The critical strain and Poisson's ratio decrease with an increase in shear modulus contrast for both the *X*- and *Y*-loading directions. Thus, composites with higher shear modulus contrasts are more prone to instabilities and show more pronounced NPR behaviors.

Next, we explore a potential application of the reported reconfigurable material for a tunable soft phononic crystal that can manipulate elastic wave propagation and filter specific frequency ranges, which, in turn, can be controlled by applied deformation. The Bloch wave analysis is performed at different

 This journal is © The Royal Society of Chemistry 2018

Published on 11 July 2018. Downloaded by Albert Ludwigs Universitaet Freiburg on 4/29/2023 10:40:51 PM.

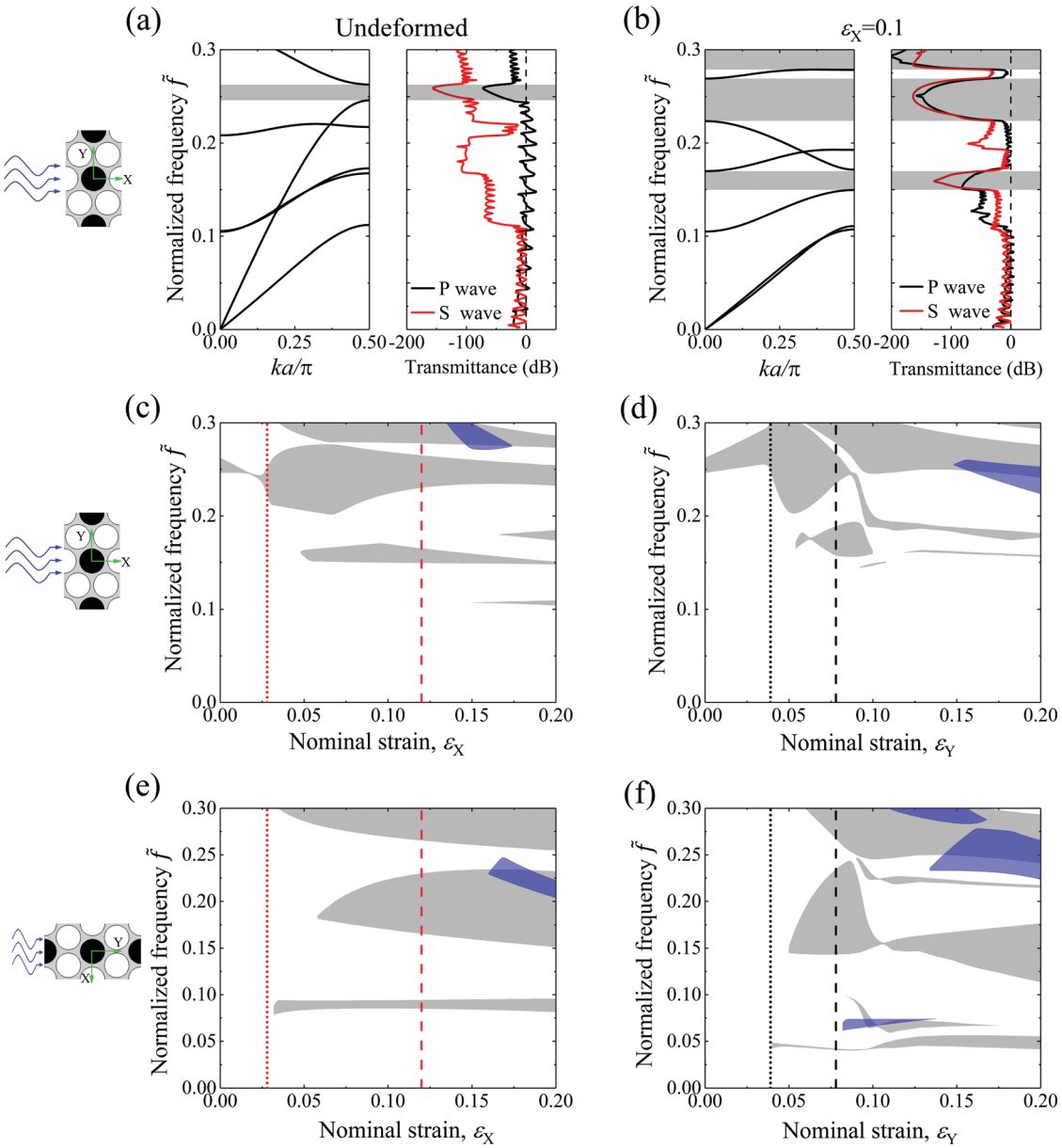


Fig. 4 (a and b) Dispersion relations and transmittance spectra for elastic waves propagating in the *X* direction in the undeformed (a) and deformed (b) states. (c–f) Evolution of the stop bands for waves propagating in the *X* (c and d) or *Y* (e and f) direction as a function of the applied strain in the *X* (c and e) or *Y* (d and f) direction. The shaded grey areas and blue areas correspond to the band gap structure of the void–inclusion–matrix composite and void–matrix system, respectively. The dotted curves and the dashed curves correspond to the critical strain of the composite and void–matrix system, respectively.

deformation levels to obtain the corresponding dispersion curves.[27] The obtained dispersion relations (a and b) and the evolution of the stop bands for waves propagating in the *X*- or *Y*-direction as a function of the applied deformation (c–f) are shown in Fig. 4. The reported frequency is normalized as $\tilde{f} = \omega a_0 \Big/ \left(2\pi\sqrt{\mu^{(m)}/\rho_0^{(m)}}\right)$, where ω is angular frequency and $\rho_0^{(m)}$ is the initial matrix density. We note that the initial density of the inclusions and matrix density are identical, namely, $\rho_0^{(i)} = \rho_0^{(m)}$.

In addition, a frequency domain analysis is performed to obtain the transmittance spectra, and 16 enlarged unit cells with periodic boundary conditions are considered in the numerical model. Shear wave (S wave) and pressure wave (P wave) are excited to evaluate the corresponding attenuation, which is calculated as $\Phi = 20\log_{10}\left|\frac{u_{out}}{u_{in}}\right|$, where u_{in} and u_{out} refer to the average displacement for the input and output enlarged unit cell, respectively.

Fig. 4a and b show the dispersion relations and corresponding transmittance spectra in the undeformed and deformed (ε_X = 0.1) states. Here, we show the results for elastic waves propagating in the *X* direction at a low frequency range $\tilde{f} \leq 0.3$. In the undeformed state, the periodic structure possesses the

Published on 11 July 2018. Downloaded by Albert Ludwigs Universitaet Freiburg on 4/29/2023 10:40:51 PM.

first band gap (*i.e.* the frequency ranges where neither pressure nor shear waves can propagate) at a lower boundary $\tilde{f} = 0.246$ with a width $\Delta\tilde{f} = 0.016$. With an applied strain $\varepsilon_X = 0.1$, the band gap shifts the lower boundary towards $\tilde{f} = 0.224$, and widens up to $\Delta\tilde{f} = 0.045$. Moreover, in the deformed state, a new band gap – that does not exist in the undeformed state – opens at a lower frequency range $\tilde{f} = 0.150$–0.170. Furthermore, the transmittance spectra shown in Fig. 4a and b demonstrate significant attenuation at the corresponding bang gap frequency ranges for both shear and pressure waves.

Next, we show the evolution of the band gaps (denoted by shaded grey areas) for an elastic wave propagating in the *X*- or *Y*-direction as a function of the applied strain in the *X* or *Y* material direction in Fig. 4c–f. We observe that the widths and locations of the band gaps are significantly influenced by applied deformation, and the new band gaps open upon reaching the instability point and pattern transformations. In the stable regime, for an elastic wave propagating in the *X*-direction, the prohibited frequency range is narrowed and shifted towards lower frequencies with an increase in the strain applied in the *X*-direction; while the applied strain in the *Y*-direction expands the band gap width and shifts it towards higher frequencies. In the post-buckling regime, the width of the band gap increases significantly. Moreover, the new band gaps are opened at low frequencies. For elastic waves propagating in the *Y*-direction, there is no band gap in the undeformed state (in the considered frequency range $\tilde{f} \leq 0.3$). However, the instability induced new patterns give rise to formation of new band gaps. For example, at the applied strain $\varepsilon = 0.2$, the structure loaded in the *X*-direction possesses two band gaps at $\tilde{f} = 0.081$–0.096 and 0.151–0.232 frequency ranges, whereas the structure loaded in the *Y*-direction possesses five band gaps at $\tilde{f} = 0.048$–0.062; 0.074–0.076; 0.139–0.178; 0.223–0.224; and 0.249–0.292. These results indicate that the reported instability-induced pattern transformations in multiphase composites holds significant potential for applications as switchable acoustic metamaterials.

For comparison, we present the evolution of the band gaps (denoted by shaded blue areas) in the void–matrix system (corresponding to the considered composite with the stiff inclusions replaced by voids) in Fig. 4c–f. The corresponding matrix volume fraction is identical to that of the void–matrix–inclusion system, namely, $c^{(m)} = 0.3$. In the void–matrix system, the instability induced pattern also opens the band gaps; however, the widths of the band gaps are significantly narrowed, and their locations are at higher frequency ranges as compared to the composite (compare the shaded blue and grey areas in Fig. 4c–f). In addition, we provide an example with the following material parameters: matrix volume fraction $c^{(m)} = 0.3$, $a_0 = 10$ mm, $\mu^{(m)} = 0.6$ MPa, $\rho_0^{(m)} = 10^3$ kg m^{-3}; and, for the composite with stiff inclusions, we consider $\mu^{(i)} = 630$ MPa and $\rho_0^{(i)} = \rho_0^{(m)}$. When elastic waves propagate in the undeformed composite in the *Y* direction, there is no band gap in the frequency range 0–600 Hz for both composites. However, at the applied deformation level of $\varepsilon_X = 0.2$, the void–matrix material opens a band gap at a frequency range 499.2–545.0 Hz, whereas the composite with stiff inclusions exhibits more remarkable band gaps at lower frequency ranges, namely, at 198.7–234.1 Hz and 370.1–568.8 Hz. This is remarkable because it is usually challenging to open band gaps at low frequency ranges.

We note that many soft materials are rate dependent, and this aspect is not included in the simulations. Therefore, the numerical predictions of the band gap are more applicable for the composites made out of phases with low damping; otherwise, these effects may shift the edges of the band gaps and affect the corresponding attenuations.[39,40] We note that the computational predictions of the band gaps in the soft single phase porous system have been experimentally demonstrated through the observed capability of significant wave attenuation in the frequency ranges controlled by deformation.[38] In addition, the examined composite exhibits significant NPR behavior and opens low frequency band gaps after its deformation exceeds the critical level; although the effective negative Poisson's ratio would result in a lower initial slope (corresponding to long waves) of the longitudinal or pressure wave branch in dispersion curves, the observed effective NPR may not be directly related to the formation of the band gaps.

Moreover, we note that the performance of the system can be potentially optimized through a selective choice of distribution, volume fractions, and shapes of stiff inclusion and voids, to give rise to specific properties, such as enhanced NPR behavior; the effect of material properties, such as shear modulus and density contrasts, and viscoelasticity, on the material performance and wave propagation properties can be also considered in future work.

To summarize, through the combination of numerical calculations and experiments on 3D printed composite samples, we demonstrate the existence of multiple stable patterns in identical composite materials with periodically arranged phases. These new instability induced patterns – tunable by the location of the stiff phases – give rise to the negative Poisson's ratio behavior. Thus, one can potentially pre-design and significantly tune the onset of instability and the associated microstructure transformations. Thus, we achieve highly tunable and switchable properties and functionalities, such as negative Poisson's ratio, and the acoustic properties of the soft composite materials. We illustrate that the reported phenomenon of reversible pattern transformations in composite materials can be utilized for the design of highly tunable phononic crystals. The reported multiphase composite material system opens new routes for the design of reconfigurable materials and devices, including acoustic switches,[38,41] actuators,[42–46] soft robotics,[47,48] and flexible electronics.[49–51]

Conflicts of interest

There are no conflicts to declare.

Appendix 1: visualization of the deformed configuration

The distinct deformed configurations of the composite loaded in the *X*-direction (a, c, e and g) or *Y*-direction (b, d, f and h) are

 This journal is © The Royal Society of Chemistry 2018

Published on 11 July 2018. Downloaded by Albert Ludwigs Universitaet Freiburg on 4/29/2023 10:40:51 PM.

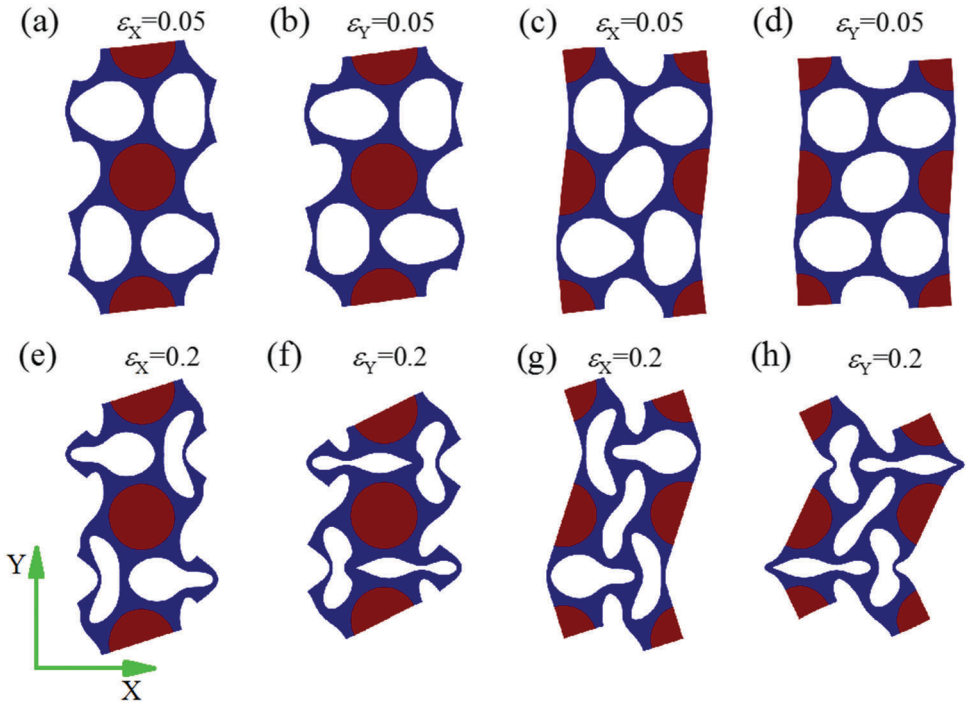


Fig. 5 Distinct pattern formation in the composite loaded in the *X*- and *Y*-material directions.

shown in Fig. 5. For completeness, we show the deformed configuration in two selections of the enlarged unit cell: the stiff inclusions located in the middle of the unit cell (a, b, e and f); and the stiff inclusions located in the corners of the unit cell (c, d, g and h) (as shown in Fig. 5). Although, the buckled patterns for the composite loaded in the *X*- or *Y*-direction are similar in the initially post-buckling deformation stage (compare the deformed configuration in Fig. 5 at $\varepsilon = 0.05$), at larger deformation levels, clearly distinct deformed void shapes are formed in the composite (compare the deformed configuration in Fig. 5 at $\varepsilon = 0.2$). Thus, the composite develops different patterns when loaded in different directions.

Appendix 2: effect of the matrix volume fraction on the composite effective Young's modulus

The dependence of the effective Young's moduli of the composite loaded in the *X*- and *Y*-material directions on the matrix volume fraction is shown in Fig. 6. The effective Young's modulus is calculated as the initial slope of the stress–strain curve in small deformations. The numerical simulations have been verified against the analytical estimates for the matrix–inclusion composite with a hexagonal periodic unit cell.[35] Here, we consider a nearly incompressible material for the matrix and inclusion, and $\mu^{(i)}/\mu^{(m)} = 10^3$. The reported effective Young's modulus is normalized by the corresponding maximum value of the modulus. We observe that the effective modulus of the composite increases with an increase in the matrix volume fraction for both *X*- and *Y*-material loading directions, and the

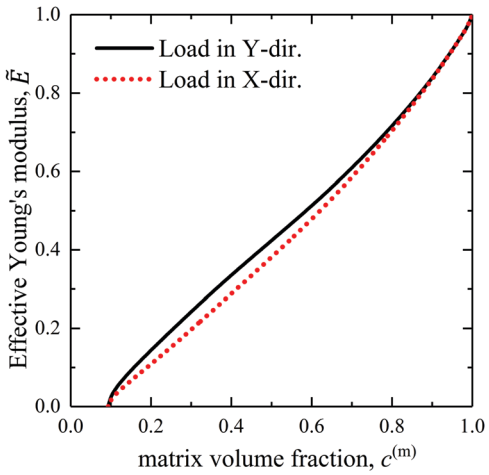


Fig. 6 Dependence of normalized effective Young's moduli of the composite loaded in the *X*- and *Y*-material directions on the matrix volume fraction.

effective modulus of the composite loaded in the *Y*-material direction is always larger than that of the composite loaded in the *X*-material direction. Moreover, for the geometrical limits, namely, $c^{(m)} = 0.093$ and 1, the normalized effective moduli attain 0 and 1, respectively.

Appendix 3: evaluation of Poisson's ratio

To evaluate the value of Poisson's ratio at different levels of applied compressive strain in experimentally observed pattern

Published on 11 July 2018. Downloaded by Albert Ludwigs Universitaet Freiburg on 4/29/2023 10:40:51 PM.

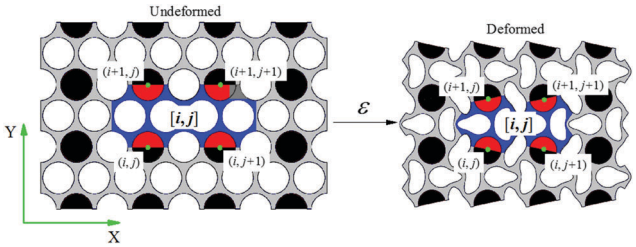


Fig. 7 Schematic diagram of the method for the experiments to calculate Poisson's ratio.

transformations, we identified the selected stiff inclusion centroids and representative elements by their row and column indices (see Fig. 7). Considering the rotational symmetry of the buckled patterns (see Fig. 2a and d), the nominal strain for each considered representative element is calculated as

$$\varepsilon_X^{[i,j]} = \frac{x^{(i,j+1)} - x^{(i,j)} + x^{(i+1,j+1)} - x^{(i+1,j)}}{4a_0} - 1, \quad (1)$$

$$\varepsilon_Y^{[i,j]} = \frac{y^{(i+1,j)} - y^{(i,j)} + y^{(i+1,j+1)} - y^{(i,j+1)}}{2\sqrt{3}a_0} - 1. \quad (2)$$

The corresponding Poisson's ratio for each representative element is defined as

$$\upsilon_{XY}^{[i,j]} = -\frac{\varepsilon_X^{[i,j]}}{\varepsilon_Y^{[i,j]}}, \quad \upsilon_{YX}^{[i,j]} = -\frac{\varepsilon_Y^{[i,j]}}{\varepsilon_X^{[i,j]}}. \quad (3)$$

Then, the average Poisson's ratio $\upsilon_{XY} = \langle \upsilon_{XY}^{[i,j]} \rangle$ and $\upsilon_{YX} = \langle \upsilon_{YX}^{[i,j]} \rangle$ for the considered 15 representative elements are computed.

Acknowledgements

This work was supported by the Israel Science Foundation (Grant No. 1550/15 and 1973/15) and the United States-Israel Binational Science Foundation (2016284). J. L. acknowledges support from a Lady Davis Fellowship. V. S. acknowledges support from a Technion postdoctoral fellowship.

References

† In our experiments, Poisson's ratio was measured by monitoring the central part of the composite samples (where the behavior is not significantly affected by the boundary effects from the sample edges) by using a high resolution digital camera allowing the position of stiff inclusion centroids to be identified. The corresponding monitored central regions of the samples are highlighted by red rectangles in Fig. 3b. The details of the evaluation of the Poisson's ratio are described in the Appendix 3.

1 I. I. Argatov, R. Guinovart-Díaz and F. J. Sabina, On local indentation and impact compliance of isotropic auxetic materials from the continuum mechanics viewpoint, *Int. J. Eng. Sci.*, 2012, **54**, 42–57.
2 G. Imbalzano, S. Linforth, T. D. Ngo, P. V. S. Lee and P. Tran, Blast resistance of auxetic and honeycomb sandwich panels: Comparisons and parametric designs, *Compos. Struct.*, 2018, **183**, 242–261.
3 A. Alderson, J. Rasburn, S. Ameer-Beg, P. G. Mullarkey, W. Perrie and K. E. Evans, An Auxetic Filter: A Tuneable Filter Displaying Enhanced Size Selectivity or Defouling Properties, *Ind. Eng. Chem. Res.*, 2000, **39**, 654–665.
4 N. Grimmelsmann, H. Meissner and A. Ehrmann, 3D printed auxetic forms on knitted fabrics for adjustable permeability and mechanical properties, *IOP Conf. Ser.: Mater. Sci. Eng.*, 2016, **137**, 012011.
5 S. Hou, T. Liu, Z. Zhang, X. Han and Q. Li, How does negative Poisson's ratio of foam filler affect crashworthiness?, *Mater. Des.*, 2015, **82**, 247–259.
6 R. Lakes, Foam Structures with a Negative Poisson's Ratio, *Science*, 1987, **235**, 1038–1040.
7 M. Sanami, N. Ravirala, K. Alderson and A. Alderson, Auxetic Materials for Sports Applications, *Procedia Eng.*, 2014, **72**, 453–458.
8 S. L. Zhang, Y.-C. Lai, X. He, R. Liu, Y. Zi and Z. L. Wang, Auxetic Foam-Based Contact-Mode Triboelectric Nanogenerator with Highly Sensitive Self-Powered Strain Sensing Capabilities to Monitor Human Body Movement, *Adv. Funct. Mater.*, 2017, **27**, 1606695.
9 A. Alderson, J. Rasburn, K. E. Evans and J. N. Grima, Auxetic polymeric filters display enhanced de-fouling and pressure compensation properties, *Membr. Technol.*, 2001, **2001**, 6–8.
10 K. Kuribayashi, K. Tsuchiya, Z. You, D. Tomus, M. Umemoto, T. Ito and M. Sasaki, Self-deployable origami stent grafts as a biomedical application of Ni-rich TiNi shape memory alloy foil, *Mater. Sci. Eng., A*, 2006, **419**, 131–137.
11 X. Ren, J. Shen, P. Tran, T. D. Ngo and Y. M. Xie, Auxetic nail: Design and experimental study, *Compos. Struct.*, 2018, **184**, 288–298.
12 A. Papadopoulou, J. Laucks and S. Tibbits, Auxetic materials in design and architecture, *Nat. Rev. Mater.*, 2017, **2**, 17078.
13 S. Shan, S. H. Kang, Z. Zhao, L. Fang and K. Bertoldi, Design of planar isotropic negative Poisson's ratio structures, *Extrem Mech. Lett.*, 2015, **4**, 96–102.
14 R. Gatt, L. Mizzi, J. I. Azzopardi, K. M. Azzopardi, D. Attard, A. Casha, J. Briffa and J. N. Grima, Hierarchical Auxetic Mechanical Metamaterials, *Sci. Rep.*, 2015, **5**, 8395.
15 M. Taylor, L. Francesconi, M. Gerendás, A. Shanian, C. Carson and K. Bertoldi, Low Porosity Metallic Periodic Structures with Negative Poisson's Ratio, *Adv. Mater.*, 2014, **26**, 2365–2370.
16 J. N. Grima and R. Gatt, Perforated Sheets Exhibiting Negative Poisson's Ratios, *Adv. Eng. Mater.*, 2010, **12**, 460–464.
17 J. N. Grima, R. Gatt, B. Ellul and E. Chetcuti, Auxetic behaviour in non-crystalline materials having star or triangular shaped perforations, *J. Non-Cryst. Solids*, 2010, **356**, 1980–1987.
18 L. Mizzi, K. M. Azzopardi, D. Attard, J. N. Grima and R. Gatt, Auxetic metamaterials exhibiting giant negative Poisson's ratios, *Phys. Status Solidi RRL*, 2015, **9**, 425–430.
19 Y. Tang, G. Lin, L. Han, S. Qiu, S. Yang and J. Yin, Design of Hierarchically Cut Hinges for Highly Stretchable and Reconfigurable Metamaterials with Enhanced Strength, *Adv. Mater.*, 2015, **27**, 7181–7190.

 This journal is © The Royal Society of Chemistry 2018

Published on 11 July 2018. Downloaded by Albert Ludwigs Universitaet Freiburg on 4/29/2023 10:40:51 PM.

20 J. N. Grima, L. Mizzi, K. M. Azzopardi and R. Gatt, Auxetic Perforated Mechanical Metamaterials with Randomly Oriented Cuts, *Adv. Mater.*, 2016, **28**, 385–389.
21 S. Babaee, J. Shim, J. C. Weaver, E. R. Chen, N. Patel and K. Bertoldi, 3D Soft Metamaterials with Negative Poisson's Ratio, *Adv. Mater.*, 2013, **25**, 5044–5049.
22 K. Bertoldi, P. M. Reis, S. Willshaw and T. Mullin, Negative Poisson's Ratio Behavior Induced by an Elastic Instability, *Adv. Mater.*, 2010, **22**, 361–366.
23 J. T. B. Overvelde, S. Shan and K. Bertoldi, Compaction Through Buckling in 2D Periodic, Soft and Porous Structures: Effect of Pore Shape, *Adv. Mater.*, 2012, **24**, 2337–2342.
24 J. Shim, S. Shan, A. Košmrlj, S. H. Kang, E. R. Chen, J. C. Weaver and K. Bertoldi, Harnessing instabilities for design of soft reconfigurable auxetic/chiral materials, *Soft Matter*, 2013, **9**, 8198.
25 J. Li, J. Shim, J. Deng, J. T. B. Overvelde, X. Zhu, K. Bertoldi and S. Yang, Switching periodic membranes via pattern trans-
formation and shape memory effect, *Soft Matter*, 2012, **8**, 10322.
26 Y. Jiang and Y. Li, Novel 3D-Printed Hybrid Auxetic Mechanical Metamaterial with Chirality-Induced Sequential Cell Opening Mechanisms, *Adv. Eng. Mater.*, 2018, **20**, 1700744.
27 K. Bertoldi and M. C. Boyce, Wave propagation and instabilities in monolithic and periodically structured elastomeric materials undergoing large deformations, *Phys. Rev. B: Condens. Matter Mater. Phys.*, 2008, **78**, 184107.
28 J. Shim, P. Wang and K. Bertoldi, Harnessing instability-induced pattern transformation to design tunable phononic crystals, *Int. J. Solids Struct.*, 2015, **58**, 52–61.
29 P. Wang, J. Shim and K. Bertoldi, Effects of geometric and material nonlinearities on tunable band gaps and low-frequency directionality of phononic crystals, *Phys. Rev. B: Condens. Matter Mater. Phys.*, 2013, **88**, 014304.
30 D. Krishnan and H. T. Johnson, Optical properties of two-dimensional polymer photonic crystals after deformation-induced pattern transformations, *J. Mech. Phys. Solids*, 2009, **57**, 1500–1513.
31 H. Cho, J. C. Weaver, E. Pöselt, P. J. in't Veld, M. C. Boyce and G. C. Rutledge, Engineering the Mechanics of Heterogeneous Soft Crystals, *Adv. Funct. Mater.*, 2016, **26**, 6938–6949.
32 M. Guttag and M. C. Boyce, Locally and Dynamically Controllable Surface Topography Through the Use of Particle-Enhanced Soft Composites, *Adv. Funct. Mater.*, 2015, **25**, 3641–3647.
33 V. Slesarenko and S. Rudykh, Towards mechanical characterization of soft digital materials for multimaterial 3D-printing, *Int. J. Eng. Sci.*, 2018, **123**, 62–72.
34 T. Frenzel, M. Kadic and M. Wegener, Three-dimensional mechanical metamaterials with a twist, *Science*, 2017, **358**, 1072–1074.
35 C. T. Sun and R. S. Vaidya, Prediction of composite properties from a representative volume element, *Compos. Sci. Technol.*, 1996, **56**, 171–179.
36 T. Mullin, S. Deschanel, K. Bertoldi and M. C. Boyce, Pattern Transformation Triggered by Deformation, *Phys. Rev. Lett.*, 2007, **99**, 084301.
37 K. Bertoldi, M. C. Boyce, S. Deschanel, S. M. Prange and T. Mullin, Mechanics of deformation-triggered pattern transformations and superelastic behavior in periodic elastomeric structures, *J. Mech. Phys. Solids*, 2008, **56**, 2642–2668.
38 S. Shan, S. H. Kang, P. Wang, C. Qu, S. Shian, E. R. Chen and K. Bertoldi, Harnessing Multiple Folding Mechanisms in Soft Periodic Structures for Tunable Control of Elastic Waves, *Adv. Funct. Mater.*, 2014, **24**, 4935–4942.
39 A. O. Krushynska, V. G. Kouznetsova and M. G. D. Geers, Visco-elastic effects on wave dispersion in three-phase acoustic metamaterials, *J. Mech. Phys. Solids*, 2016, **96**, 29–47.
40 M. A. Lewińska, V. G. Kouznetsova, J. A. W. van Dommelen, A. O. Krushynska and M. G. D. Geers, The attenuation performance of locally resonant acoustic metamaterials based on generalised viscoelastic modelling, *Int. J. Solids Struct.*, 2017, **126–127**, 163–174.
41 C. Yuan, X. Mu, C. K. Dunn, J. Haidar, T. Wang and H. J. Qi, Thermomechanically Triggered Two-Stage Pattern Switching of 2D Lattices for Adaptive Structures, *Adv. Funct. Mater.*, 2018, 1705727.
42 R. Liu, X. Kuang, J. Deng, Y.-C. Wang, A. C. Wang, W. Ding, Y.-C. Lai, J. Chen, P. Wang, Z. Lin, H. J. Qi, B. Sun and Z. L. Wang, Shape Memory Polymers for Body Motion Energy Harvesting and Self-Powered Mechanosensing, *Adv. Mater.*, 2018, **30**, 1705195.
43 D. Yang, B. Mosadegh, A. Ainla, B. Lee, F. Khashai, Z. Suo, K. Bertoldi and G. M. Whitesides, Buckling of Elastomeric Beams Enables Actuation of Soft Machines, *Adv. Mater.*, 2015, **27**, 6323–6327.
44 C. Yuan, D. J. Roach, C. K. Dunn, Q. Mu, X. Kuang, C. M. Yakacki, T. J. Wang, K. Yu and H. J. Qi, 3D printed reversible shape changing soft actuators assisted by liquid crystal elastomers, *Soft Matter*, 2017, **13**, 5558–5568.
45 D. K. Patel, A. H. Sakhaei, M. Layani, B. Zhang, Q. Ge and S. Magdassi, Highly Stretchable and UV Curable Elastomers for Digital Light Processing Based 3D Printing, *Adv. Mater.*, 2017, **29**, 1606000.
46 N. Kellaris, V. Gopaluni Venkata, G. M. Smith, S. K. Mitchell and C. Keplinger, Peano-HASEL actuators: Muscle-mimetic, electrohydraulic transducers that linearly contract on activation, *Sci. Robot.*, 2018, **3**, eaar3276.
47 B. Mosadegh, P. Polygerinos, C. Keplinger, S. Wennstedt, R. F. Shepherd, U. Gupta, J. Shim, K. Bertoldi, C. J. Walsh and G. M. Whitesides, Pneumatic Networks for Soft Robotics that Actuate Rapidly, *Adv. Funct. Mater.*, 2014, **24**, 2163–2170.
48 E. Acome, S. K. Mitchell, T. G. Morrissey, M. B. Emmett, C. Benjamin, M. King, M. Radakovitz and C. Keplinger, Hydraulically amplified self-healing electrostatic actuators with muscle-like performance, *Science*, 2018, **359**, 61–65.
49 M. Zarek, M. Layani, I. Cooperstein, E. Sachyani, D. Cohn and S. Magdassi, 3D Printing of Shape Memory Polymers

Published on 11 July 2018. Downloaded by Albert Ludwigs Universitaet Freiburg on 4/29/2023 10:40:51 PM.

for Flexible Electronic Devices, *Adv. Mater.*, 2016, **28**, 4449–4454.

50 J. Deng, X. Kuang, R. Liu, W. Ding, A. C. Wang, Y.-C. Lai, K. Dong, Z. Wen, Y. Wang, L. Wang, H. J. Qi, T. Zhang and Z. L. Wang, Vitrimer Elastomer-Based Jigsaw Puzzle-Like Healable Triboelectric Nanogenerator for Self-Powered Wearable Electronics, *Adv. Mater.*, 2018, **30**, 1705918.

51 H. Fu, K. Nan, W. Bai, W. Huang, K. Bai, L. Lu, C. Zhou, Y. Liu, F. Liu, J. Wang, M. Han, Z. Yan, H. Luan, Y. Zhang, Y. Zhang, J. Zhao, X. Cheng, M. Li, J. W. Lee, Y. Liu, D. Fang, X. Li, Y. Huang, Y. Zhang and J. A. Rogers, Morphable 3D mesostructures and microelectronic devices by multistable buckling mechanics, *Nat. Mater.*, 2018, **17**, 268–276.

 This journal is © The Royal Society of Chemistry 2018